Simulating the roles of crevasse routing of surface water and basal friction on the surge evolution of Basin 3, Austfonna ice-cap

Yongmei Gong[1], Thomas Zwinger[2], Jan Åström[2], Bas Altena[3], Thomas Schellenberger[3], Rupert Gladstone[4], John C. Moore[5]

[1]Institute for Atmospheric and Earth System Research, University of Helsinki, Helsinki, 00560, Finland

[2]CSC – IT Center for Science Ltd., Espoo, 02101, Finland

[3]Department of Geosciences, University of Oslo, Oslo, 0371, Norway

[4]Arctic Center, University of Lapland, Rovaniemi, 96100, Finland

[5]College of Global Change and Earth System Science, Beijing Normal University, Beijing, 100875, P.R. China

Correspondence to: Yongmei Gong (yongmei.gong@helsinki.fi)

Abstract. The marine-terminating outlet in Basin 3, Austfonna ice-cap has been accelerating since the mid-1990s. Step-wise multiannual acceleration associated with seasonal summer speed-up events was observed before the outlet entered the basin-wide surge in autumn 2012. We use multiple numerical models to explore hydrologic activation mechanisms for the surge behavior. A continuum ice dynamic model is used to invert basal friction coefficient distributions using the control method and observed surface velocity data between April 2012 and July 2014. This provides an input to a discrete element model capable of simulating individual crevasses, with the aim of finding locations where summer melt water enters the glacier and reaches the bed. The possible flow paths of input surface melt water at the glacier bed and basal melt water are calculated according to the gradient of the hydraulic potential.

The inverted friction coefficients show the 'unplugging' of the stagnant ice front and expansion of low friction regions before the surge reached its peak velocity in January 2013. Crevasse distribution reflects to a high degree the basal friction pattern. The melt water reaches the bed through the crevasses located above the margins of the sub-glacial valley and the basal melt that is generated mainly by frictional heating flows either to the fast flowing units or potentially gets accumulated in an over-deepened region. Based on these results, the mechanisms facilitated by basal melt water production, surface melt water and crevasse opening, for the surge in Basin 3 are discussed.

1 Introduction

Austfonna ice-cap, located on Nordaustlandet in the Svalbard archipelago, is the largest ice mass in the Eurasian Arctic in terms of area (7800 km^2) (Moholdt and Kääb, 2012). Basin 3 is one of its southeastern basins containing a marine-terminating outlet glacier. The glacier is largely marine-grounded to as much as 150 m below sea level and is known to have surged around 1850-1870 (Dowdeswell et al., 1986).

The northern flow unit of the outlet glacier experienced long-term acceleration since the mid-1990s (Dowdeswell et al., 1986) along with stepwise inter-annual accelerations since 2008. These short-lived summer speed-up events occurred during the surface melt season (Dunse et al., 2015). The southern corner of Basin 3 accelerated to about 290 m a^{-1} in spring 2008 but had decelerated again by spring 2011 (Gladstone et al., 2014). However high velocities were again observed in the same area during spring 2012 which subsequently gradually increased to ~1800 m a^{-1} after the summer melt season and before a basin-

wide surge took place in autumn 2012 (Dunse et al., 2015). The surge reached its peak in January 2013 with a maximum velocity of ~6500 m a^{-1}.

The 130-140 year long quiescent phase of Basin 3 is similar to other Svalbard glaciers, but the two decades long accelerating phase of the northern flow unit exceeds those of other glaciers such as the 7-11 years of Monacobreen (Strozzi et al., 2002). The step-wise multi-annual acceleration observed since 2008, associated with seasonal summer speed-up events, is also exceptional from other surging glaciers in Svalbard. Similar melt season speed-up events have been observed in Greenland, and provides evidence for rapid, large-scale, dynamic responses of the ice sheet to climate warming (Sundal et al., 2011; van de Wal et al., 2008; Zwally et al., 2002). Sundal et al (2011) pointed out that a simple model of basal lubrication alone could not simulate the fast flowing manner of the glaciers on Greenland ice sheet, and that an improved understanding of sub-glacial drainage would be essential for model studies to capture ice dynamic responses to climate warming. This applies also to the surge in Basin 3, which requires a mechanism involving both thermal and hydrologic changes to explain the inter-annual and seasonal accelerations (e.g. Dunse et al., 2015; Gladstone et al., 2014).

The glacier in Basin 3 (recently named Storisstraumen) is polythermal, with a maximum ice thickness of 567 m, sufficient to raise internal ice temperatures to the pressure melting point (pmp) (Dunse et al., 2011). Where the ice is thinner, closer to the margins, the ice is probably frozen to the bed except under fast flowing outlets. In principle the surge of polythermal glaciers can be explained by a soft-bed mechanism with some constraints for the initiation, such as the unfreezing of the cold bed by the evolution of the thermal regime or by the input of melt water from englacial channels (Clark, 1976; Lingle and Fatland, 2003; Robin, 1955).

Gladstone et al. (2014) suggest soft-bed sliding mechanisms involving feedbacks in the hydrological system at the ice-till interface responding to penetration of surface melt to explain the summer speed-up events observed since 2008. Surface meltwater can penetrate cold and polythermal glacier ice in High Arctic glaciers and the Greenland ice sheet through moulins and fractures that cut down all the way to the glacier bed (e.g. Benn et al., 2009; Copland et al., 2003; van de Wal et al., 2008; Zwally et al., 2002). Water-filled crevasses can penetrate to the glacier bed regardless of ice thickness or crevasse spacing as long as the tensile stress acting normal to the crevasse exceeds about 100kPa (Boon and Sharp, 2003; van der Veen, 1998). Bougamont et al (2014) investigated the sensitivity of the basal hydrology system in the Russell glacier catchment to the volume of surface melt delivered to the bed, finding increases in surface melt volumes lead to faster summer flow.

Dunse et al. (2015) has suggested a “hydro-thermodynamic” feedback whereby summer meltwater penetrating to the bed is not considered a purely external forcing to the system: meltwater penetrating crevasses to reach the bed enhances basal processes such as lubrication and sediment deformation resulting in enhanced ice flow and potentially an increase in extensional stress, which may in turn cause increased crevasse formation over a wider area, routing more melt water down to the bed.

These earlier studies highlight the importance of time-evolving basal temperature and friction, which are strongly influenced by the evolution of a basal hydrology system. The basal hydrology system can be fed both by in situ melting and by surface meltwater, and has the capacity to not only directly cause sliding but also to alter the thermal regime and hence deformational flow.

Previous crevasse modeling studies simulate the formation of fractures as a continuous process. They treat the development of cracks on a macroscopic scale by either using simplified parameterization of fracturing effects via variables such as depth

of crevasse (Cook et al., 2014; Nick et al., 2010, 2013; Weertman, 1973) or using Continuous Damage Mechanics (CDM), which simulates the continuous process from micro-scale cracks to macro-scale crevasses (Albrecht and Levermann, 2014; Bassis and Ma, 2015; Borstad et al., 2012, 2016; Krug et al., 2014). In this study we take a different approach and apply a discrete element model (Åström et al., 2013, 2014) capable of simulating crevasse formation as a microscopic scale discrete process in addition to the continuum ice dynamics models. The discrete element model (HiDEM) is used to determine the locations of the crevasses penetrating though the full thickness of the glacier whereby surface water may reach the bed.

In Sect. 2 we present the observational data used for setting up the simulations and validating the results. In Sect. 3 we present the methodology. We use a continuum ice dynamic model to invert the basal friction field from approximately monthly observations of ice surface velocities between April 2012 and July 2014. This basal friction field then acts as a boundary condition for basal sliding in our discrete element model that simulates crevasse distribution in the lower part of Basin 3 for particular points in time. In Sect. 4.1 we firstly investigate the evolution of the basal conditions in Basin 3 during and after the peak of the surge. In sect. 4.2 we present the modeled crevasse distributions before and after maximum surge velocity and validate the latter with crevasse map derived from satellite imagery. In Sect. 4.3 we locate the crevasses that reach the bed, calculate basal melt rates and estimate the flow path of the basal water. In Sect. 5 we discuss the mechanisms facilitated by basal melt water production, surface melt water and crevasses opening for the surge that occurred in Basin 3. In Sect. 6 we summaries the key findings of the study and present conclusions.

2 Observations

2.1 Surface and bedrock topography data

Bedrock elevation (Dunse, 2011) was derived by point-wise subtracting the measured ice thickness from a 250 m resolution surface elevation that is derived from a Norwegian Polar Institute (NPI) 1:250 000 topographic map published in 1998 and InSAR data of Austfonna acquired in 1995-96 (Unwin and Wingham, 1997). The ice thickness used for generating bedrock elevation was based on airborne radio echo sounding (RES; Dowdeswell et al., 1986) supplemented with two RES data sets from 2008 (Vasilenko et al., 2009). Marine bathymetry (2 km horizontal resolution) was from the International Bathymetry Chart of the Arctic Ocean, Version 2.0 (Jakobsson et al., 2008). Bathymetry and inland bedrock elevation were combined by using an interactive gridding scheme to eliminate the mismatch along the southern and northwest coast line (Dunse, 2011). We assume that bedrock elevation does not have any significant changes over decadal time scales, and use it with a set of updated surface elevation data. The surface elevation was derived from Cryosat altimetry data acquired during July 2010 – December 2012 (McMillan et al., 2014). McMillan et al. (2014) grouped measurements acquired over a succession of orbit cycles that are within 2-5 km^2 geographic regions.

We point out several bed topography features (Fig. 1b) that are important to the investigation here. The sub-glacial hill located at roughly 700 km E and 8850 km N rises to about 250 m above sea level. A corresponding, but smaller magnitude, bedrock maximum exists at the opposite side of Basin 3, approx. 15-20 km southwest of the aforementioned hill. A subglacial valley runs between these bedrock maxima, marked as SV Fig.1b, and extends several tens of km upstream and downstream. The minimum bedrock height for Basin 3 is within an over-deepening in the lower part of the valley, marked as OD on Fig.1b. The importance of these features is discussed in more detail in Sect. 4 and 5.

2.2 Surface velocity data

We used velocity time series maps (April 2012-July 2014) generated from TerraSAR-X (TSX) satellite synthetic aperture radar (SAR) scenes, (Table 1; Schellenberger et al., 2017, in review) as the input surface velocity data for basal friction coefficient inversion. These maps were based on original 2m resolution TSX scenes provided by the German Aerospace Center (DLR) covering only the lower part of Basin 3 (Fig. 1a). To generate the final velocity maps for the times between two successive TSX images, which were geocoded using a DEM of Austfonna (Moholdt and Kääb, 2012), we needed to use displacement maps. The displacement maps between two consecutive acquisitions were determined using cross-correlation of the intensity images (Strozzi et al., 2002).

The coverage of the TSX velocity was smaller than the model domain used by our ice dynamic model (Fig. 1a). Therefore we stitched the TSX data on top of two background velocity fields with larger coverage depending on the acquiring time. The TSX data derived during 19 April 2012 – 28 December 2012 was stitched with velocity snapshot from ERS-2 (European Remote Sensing Satellite 2) SAR observation acquired in March to April 2011(Gladstone et al., 2014; Schäfer et al., 2014); and the TSX data derived after 28 December 2012 was stitched with velocity snapshot from Landsat-8 imagery acquired in April 2013. We then applied a row-wise recalculation of the velocity value for the grid points on the model mesh that were upstream from the TSX velocity map coverage (Fig. 1a) to create a smoother transition from TSX velocity map to the background velocity map. The recalculation was carried out by weighting the background velocity data and TSX velocity data according to the distance between the column indices of the targeting grid point and the column indices of the first grid point that had value from TSX velocity map on the same row.

The velocity recalculated for the upstream area was simply to avoid numerical instability that might appear at the boundary between the TSX and background velocities. So as not to bias the crevasses distribution calculation, we confined the discrete element model domain to a smaller region close to the ice front, which was fully covered by TSX velocity map and far away from this transition zone (Fig. 1a).

3 Methodology

3.1 Basal friction inversion in the ice flow model

The continuum ice dynamic model we used is Elmer/Ice, an open-source finite element model for computational glaciology. In this study, the simulations with Elmer/Ice were carried out by considering a gravity-driven flow of incompressible and non-linearly viscous ice flowing over a rigid bed. Some of the governing equations are presented below. More details can be found in Gagliardini et al.(2013).

The ice flow was computed by solving the unaltered full-Stokes equations, which express the conservation of linear momentum:

$$\nabla \cdot \boldsymbol{\sigma} + \rho_i \boldsymbol{g} = \nabla \cdot \boldsymbol{\tau} - \nabla \mathrm{p} + \rho_i \boldsymbol{g} = \mathbf{0}, \quad (1)$$

and the mass conservation for an incompressible fluid:

$$\nabla \cdot \boldsymbol{u} = \mathrm{tr}(\dot{\boldsymbol{\varepsilon}}) = 0, \quad (2)$$

in which ρ_i is the ice density, $\boldsymbol{g} = (0,0,-g)$ the gravity vector, $\boldsymbol{u} = (u,v,w)$ the ice velocity vector, $\boldsymbol{\sigma} = \boldsymbol{\tau} - p\boldsymbol{I}$ the Cauchy stress tensor with $p = -tr(\boldsymbol{\sigma})/3$ the isotropic pressure, $\boldsymbol{\tau}$ the deviatoric stress tensor, $\boldsymbol{I}$ the identity matrix and $\dot{\boldsymbol{\varepsilon}}$ the strain-rate tensor.

The constitutive relation for ice rheology was given by Glen's flow law (Glen, 1955):

$$\boldsymbol{\tau} = 2\mu\dot{\boldsymbol{\varepsilon}}, \tag{3}$$

where the effective viscosity μ is defined as

$$\mu = \frac{1}{2}(EA)^{-\frac{1}{n}}\dot{\varepsilon}_e^{\frac{1-n}{n}}, \tag{4}$$

in which $n = 3$ is the Glen's flow law exponent, $\dot{\varepsilon}_e^2 = tr(\dot{\boldsymbol{\varepsilon}}^2)/2$ is the square of the second invariant of the strain rate tensor; E is the enhancement factor; A is the rate factor calculated via Arrhenius law:

$$A = A_0 \exp\left(-\frac{Q}{RT'}\right), \tag{5}$$

$$T' = T + \beta p, \tag{6}$$

where A_0 is the pre-exponential constant, Q is the activation energy, $R = 8.321\ J\ mol^{-1}\ K^{-1}$ is the universal gas constant and T' is the temperature relative to pressure melting.

The upper surface, $Z_s\ (x, y, z)$, evolved with time in transient simulations through an advection equation:

$$\frac{\partial Z_s}{\partial t} + u_s\frac{\partial(Z_s)}{\partial x} + v_s\frac{\partial(Z_s)}{\partial y} - w_s = M_s, \tag{7}$$

where (u_s,v_s,w_s) is the surface velocity vector obtained from the Stokes solution , M_S is the meteoric accumulation/ablation rate and s is the surface elevation.

For all the simulations carried out in this study a linear relation linking basal shear stress, τ_b, to basal velocity, $\boldsymbol{u}_b = (u_b,v_b,w_b)$, was applied:

$$\boldsymbol{\tau}_b = -C\boldsymbol{u}_b, \tag{8}$$

in which $C = 10^{\alpha}$ is the basal friction coefficient.

We performed inverse modeling of basal friction coefficient distributions from all the surface velocity observation snapshots using Elmer/Ice based on the control method (MacAyeal, 1993; Morlighem et al., 2010) implemented in Elmer/Ice by Gillet-Chaulet et al (2012). The inverse modeling determined the spatial distribution of the exponent, α, of the basal friction coefficient, C, *by* minimizing the mismatch between modeled and observed surface velocity as defined by a cost function:

$$J_o = \int_{\Gamma_s}\frac{1}{2}(|\boldsymbol{u}_{mod}| - |\boldsymbol{u}_{obs}|)^2\, d\Gamma, \tag{9}$$

where $|u_{mod}|$ and $|u_{obs}|$ are the magnitude of the modeled and observed horizontal surface velocities. The mismatch in the direction of the velocity components is ignored. And only a match of velocity magnitude is optimized.

A Tikhonov regularization term penalizing the spatial first derivatives of α was used to avoid over fitting:

$$J_{reg} = \frac{1}{2}\int_{\Gamma_b}(\frac{\partial\alpha}{\partial x})^2 + (\frac{\partial\alpha}{\partial y})^2 d\Gamma, \tag{10}$$

such that the total cost function is now written as:

$$J_{tot} = J_0 + \lambda J_{reg}, \tag{11}$$

where λ is a positive ad-hoc parameter. We adopted the same procedure as in Gillet-Chaulet et al. (2012) to find the optimal λ value.

As introduced in Sect.1, ideally, a soft-bed sliding mechanism needs to be presented in the simulation to be able to capture the surging behavior. However, as the main goal of this study is only to find a model approach to locate the surface melt water input sources, a linear basal sliding relation solved with an inverted parameter (C) which reflects the observation quite well (Fig. 2) is good enough to serve the purpose.

The temperature distribution was calculated according to the general balance equation of internal energy written as:

$$\rho_i c_v \left(\frac{\partial T}{\partial t} + u \cdot \nabla T\right) = \nabla \cdot (\kappa \nabla T) + D{:}\sigma, \quad (12)$$

where $\kappa = \kappa(T)$ and $c_v = c_v(T)$ are the heat conductivity and specific heat of ice, respectively. D:σ represents the amount of energy produced by ice deformation. The upper value of the temperature T is constrained by the pressure melting point T_m of ice.

The Dirichlet boundary condition at the upper surface, T_{surf}, was prescribed as:

$$T_{surf} = T_{sea} + \Gamma z_s, \quad (13)$$

where T_{surf} is the surface ice temperature, $T_{sea} = -7.68$ °C is the mean annual air temperature at sea level estimated from two weather stations on Austfonna during 2004 and 2008 (Schuler et al., 2014) and four weather stations on Vestfonna during 2008 and 2009 (Möller et al., 2011), $\Gamma = 0.004$ K m^{-1} is the lapse rate (Schuler et al., 2007).

An initial guess of the ice temperature, T_{init}, was given by:

$$T_{init} = T_{surf} + \frac{q_{geo}}{\kappa} d, \quad (14)$$

where $q_{geo} = 40.0$ mW m^{-2} is the geothermal heat flux (Dunse et al., 2011) and d the distance from the upper surface.

Spatially varied ice temperatures (T) snapshots in the flow solution were accommodated using an iterative process which includes four parts: i) Invert C_{invert} for the first time with either an initial guess of C_{init} and T_{init} or the previously inverted C_{prev} and T_{prev}; ii) Carry out steady state simulation for only thermodynamics to calculate T_{invert} using the velocities obtained from the inversion; iii) Do the inversion again using C_{invert} and T_{invert} derived from the previous simulations; iv) Repeat the iteration until the differences in C_{invert} and T_{invert} between two successive iterations fall below a given threshold. More details about the interactive process can be found in Gong et al. (2016).

All the thermodynamic-coupled inversions were done sequentially in chronological order with a transient simulation after each inversion to evolve the geometry for the next inversion. A month of geometry evolution starts with the C field inverted from the first velocity map acquired during that month to evolve the glacial geometry for 30 days with temporal resolution of half a day, and mean 1990-2000 surface mass budget (SMB) forcing from the regional climate model HIRHAM 5 (Christensen et al., 2007). In the case of acquisition time gaps (Table 1; mostly after August 2013) transient simulations were carried out for the length of the gap with the latest C distribution and temporal resolution of one day.

All simulations were computed on an unstructured mesh over Basin 3 generated with the open source software GMSH (Geuzaine and Remacle, 2009). The element size of the mesh increased from ~150 m at the glacier terminus to 2500 m at the back of the basin. The 2D mesh was then vertically extruded between the interpolated bedrock and surface elevation into 10 equally spaced terrain-following layers to form a three-dimensional (3D) mesh.

A fixed calving front criterion was adopted in all the simulations in this study due to the lack of ice thickness information corresponding to the observed calving front positions after 2011. The criterion assumed that the calving front was always grounded with a positive height above floatation, which reflected the observation at the terminus in Basin 3. As the near-frontal region was not confined between lateral walls we would not expect significant impact of different calving front

positions on longitudinal stress gradient upstream, i.e. the migration of calving front would have less impact on the basal shear stress distribution in the upstream area than the uncertainties brought by the observed ice velocity or the lack of ice thickness information at the calving front. The fixed calving front criterion would not distort the basal shear stress calculation at the ice terminus neither, as the basal resistance there was already low in 2012. However as the ice front in the simulation did not migrate the calving flux might be biased.

3.2 Crevasse distribution calculation by a discrete element model

HiDEM is a model for fracture formation and dynamics. In HiDEM, an ice body is divided into discrete particles connected by massless beams. The version of HiDEM used here is purely elastic, rather than visco-elastic (Åström et al., 2013). The elastic version is sufficient for the purpose of locating fractures governed by glacier geometry and basal friction. If the initial state of a model glacier is out of elastic equilibrium, deformation within the ice will appear as a result of Newtonian dynamics. The explicit scheme for simulating the Newtonian dynamics and the elastic modulus can be found in Riikilä et al. (2015). We use a Young's modulus Y = 2.0 GPa and a Poisson ratio $\nu \approx 0.3$ for the modeled ice here. The modeled ice fractures if the stress on a beam exceed a fracture stress criterion (stretching or bending). The fracture stress is ~ 1MPa.

All the simulations in this study were carried out with 30 m spatial resolution (the particles are uniformly shaped and initially uniformly spaced). We used a time step length of 10^{-4} s, and ran a simulation until the glacier began to approach an equilibrium state. Compared to viscous flow, elastic deformation and fracturing processes are very rapid, and a typical simulation covers about ~ 10 minutes of glacier dynamics. At the end of a simulation, a crevasse field has formed. HiDEM reflects the instantaneous stress field calculated for the time of the input boundary conditions without consideration of any pre-existing damage or advection. Further details of the model, including sensitivity of the chosen parameters to the model results are discussed in Åström et al. (2013, 2014) and Riikilä et al. (2015). All parameters were set beforehand.

The simulations were set up with input data from marine bathymetry, bedrock topography, C field, and the surface topography. We selected two C snapshots inverted from velocity data observed in 18-29 August 2012 (C_{pre}) and 16-27 August 2013 (C_{post}) (Fig. 2) as boundary condition for basal sliding in HiDEM. Those dates were chosen to model the crevasse distribution after the summer melt season before and after the peak in surge velocities observed in January 2013. The computations were carried out on an HPC cluster using typically 500 computing cores for a few hours.

3.3 Crevasse map

We created a crevasse map from satellite imagery to validate our modeled crevasse distribution. The map was generated from a Landsat 8 image acquired on 4th August 2013 using the Radon-transform technique (Petrou and Kadyrov, 2004; Toft and Sørensen, 1996). We experimented with crevasse maps created from various different satellite sensors (Landsat 7, Landsat 8, ASTER, Sentinel-2), but here we used only the Landsat 8 scene which combines good spatial coverage with high radiometric quality.

The Radon-transform has been demonstrated to be efficient in detecting along flow features (Roberts et al., 2013), but can also be used for complex flow patterns, like the one in Basin 3 which has a wide range of crevasse orientations. The advantages of the Radon-transform over other detecting methods are that crevasse patterns can be extracted where edge detectors methods (Bhardwaj et al., 2015; Wesche et al., 2013) would fail, and also that it is more robust than frequency-domain methods

(Sangwine and Thornton, 1998) in detecting crevasses from incomplete coverage due to cloud coverage, image borders or the calving front.

In this study we followed a similar approach as Roberts et al. (2013), but used a more robust implementation and a different post-processing procedure. Firstly, the satellite image was pre-processed with a Laplacian-filter to prioritize the high frequencies, e.g. to sharpen the edges of surface features. We performed the Radon-transform, $R(p, \theta)$ on 300 m×300 m subsets of the satellite image, and project the image intensity $I(x, y)$ along lines with tangent vectors oriented at θ to the x-axis and offset by a perpendicular distance, p, from the origin (Toft and Sørensen, 1996):

$$R(p,\theta) = \int_{-\infty}^{\infty}\int_{-\infty}^{\infty} I(x,y)\delta(-x\,sin\theta + y\,cos\theta - p)dxdy, \quad (15)$$

where the 2D integration is restricted by the Dirac delta function, $\delta(-x\,sin\theta + y\,cos\theta - p)$, to the appropriate straight line in the x-y plane. The range of the transform coordinates is a half circle ($0 \le \theta < \pi$) and p is the spatial integral ranging over the domain of the subset of the image. The result of the transform was a 2D feature space at different azimuthal orientations (θ). To capture both small and big crevasses, we re-sampled the image intensity $I(x, y)$ in each 300m×300m image subset with a resolution of 2 pixels and again implement a weighted Radon-transform function, where a mask over the subset was used to remove features like image borders, clouds, ocean etc. The resulting Radon transformation of a subset was again a two dimensional subset. Then the standard deviation at each orientation was used to extract the response for elongated texture:

$$s(\theta) = \sqrt{\frac{\sum_{i=-P}^{P}\left(R(i,\theta) - \bar{R}(\theta)\right)^2}{N+1}} \quad (16)$$

Here the overbar denotes the mean and N denotes the amount of steps within the domain of p. Finally, a running median filter with a spacing of two ($\Delta = 1°$) was used to remove noise:

$$\tilde{s}(\theta) = median\{s(\theta - \Delta), \cdots, s(\theta + \Delta))\} \quad (17)$$

The results of the procedure were maps showing the dominating azimuthal orientations (θ) of the crevasse clusters (Fig. 3a) and their response ($\tilde{s}(\theta)$) (Fig. 3b) in each 300 m×300 m window. We wish to compare the simulated crevasse pattern from HiDEM with these results from the observation. To identify crevasse zones and their alignment in the satellite images we process an empty image array for each 300 m×300 m window with randomly seeded high intensity values. Then a simplified line integral convolution was applied to add each element of the image to its local neighbors, weighted by a kernel. The kernel has an elongated shape. The orientation of the shape is dependent on θ at the underlying position. The response of the kernel (the intensities within) was dependent on $\tilde{s}(\theta)$ extracted from the underlying position. The resulting image is shown in Fig. 3c, and will be compared with the modeled crevasses distribution visually as well as using the statistical Kappa method.

4 Results

4.1 Basal friction evolution

Figure 2 shows that the relative errors between the modeled and observed surface velocity magnitude for both the 18-29 August 2012 and the 16-27 August 2013 snapshots are the lowest over the fast flowing region (< 5%; Fig. 2), the areas mostly moving by basal sliding. The root-mean-squared difference of the modeled surface velocity magnitude fields in the TXS data

covered region (Fig. 1) for these two time periods are 65.0 and 190.9 m a^{-1}, respectively. As we are mostly interested in the ice dynamics of the fast flowing area, these errors are acceptable for the crevasse formation simulations.

Figure 4 shows the friction pattern of the region that is fully covered by TSX velocity observations between April 2012 and July 2014, spanning the period of the Basin 3 peak surge velocities in January 2013. To make the pattern of the *C* distribution clearer we plotted the common logarithm of C ($\log_{10}$ (C)). Figure 4a shows a clear expansion of low friction area ($\log_{10}$ (C) ≤ -3.5) both inland and to the frontal region in the southern basin before the glacier enters the peak of the surge.

In 2011 the low friction patches in the central and southern basin were disconnected from the inland region and also lie behind a stagnant terminus. Before May 2012, the enlarged low friction area in both northern and southern glacier terminus did not expand across the flat glacier bed in between them, which might impose some topographic restriction to the expansion of the fast flow. After the summer melt season (August 2012) the stagnant frontal region shrank to the glacial terminus which might have thinned to reach a condition close to floatation (McMillan et al., 2014). During this period the low friction area underneath the southern part expanded further inland and became connected to the northern low friction area. In January 2013 the glacier entered a basin-wise surge and the low friction area also expanded across the entire width of the basin near the calving front with a few particularly deep minima ($\log_{10}$ (C) ≤ -5.5; almost vanishing friction) in the south (Fig. 4b).

After January 2013 the basal friction pattern in northern basin remained almost stable. The almost vanishing friction area ($\log_{10}$ (C) ≤ -5.5) in the southern frontal region gradually shrank back inland away from the terminus.

4.2 Crevasse distribution and validation

All the fractures calculated by HiDEM are wider than 0.055m, of which we regard as crevasses in this study. The fractures marked with black dots (Fig. 5b; in both upper left and lower left corner of the domain) are generated by boundary effects due to the limited domain. Although they might be deep enough to cut through the full depth of the ice we regard them as artificial crevasses. They are irrelevant to the water routing and surge processes we focus on in this paper thus are exclude from the comparison in this section and the water routing calculation in Sect. 4.3.

The crevasse map created by the Radon-transform shows a highly crevassed glacial lower region, which comprise sections with crevasses of different orientation (Fig. 3). Transverse crevasses that are almost perpendicular to the flow direction can be found in both northern and southern flow units (Fig. 1b), reflecting large longitudinal tensile stress after dramatic acceleration. However, the detection intensity of the crevasse in the northern flow unit is rather weak. The terminus between the northern and middle flow units has a mixture of crevasses with orientations perpendicular to each other indicating the expansion and merging of the two flow units. Marginal crevasses can be found above the sub-glacial valley (Fig. 1b) margins parallel to the local flow direction reflecting lateral shear stresses and longitudinal compressive stress caused by the presence of the valley margins.

The modeled crevasse distribution reflects the broad features the basal friction pattern (Fig. 5b). A high crevasse density is generated in areas with large tensile stress caused by extending flow on the lower part of basin 3, as well as at shear margins between low and high friction areas. The orientation of the modeled crevasses above the sub-glacial valley margins agrees with the observation (Fig. 5b). However orientations of most of the modeled crevasses in the middle upper area have a ~60° mismatch with the satellite image (Fig, 5c) and the modeled crevasse density at the frontal area of the southern and northern flow units are larger than those in the observationally derived map.

Although the visual comparison between the two maps shows a general agreement (Fig 5c), estimation of statistical quality of the simulated crevasse field with the observationally estimated map is necessary. We calculated the Kappa coefficient (K) (Wang et al., 2016) to quantify the agreement, but this is not trivial as almost any two maps will be significantly different with large sample size (> 62483) (Monserun and Leemans, 1992). We achieve moderate agreement (Cohen, 1960), (K = 0.45) when re-sampling the two maps with a 1.5 × 1.5 km smoothing window and substantial agreement (K = 0.71) with a 4.6 × 4.6 km smoothing window. When including the artificial crevasses (defined at the beginning of the section) the agreement is only fair (K ~= 0.30) for both re-sample windows. A variety of reasons can explain the resolution dependency of the results of the Kappa method: the ice dynamics model cannot advect crevasses, hence many crevasses in the image that in reality were created further upstream were simply not present in the simulation; crevasse densities are very variable; and the observationally derived map is not a perfect representation of reality.

To investigate the crevasse distribution after the summer melt season in 2012, we used C_{pre} and the corresponding geometry within HiDEM. The configuration produced more crevasses in the frontal region of the northern flow unit than in the southern flow unit and almost no crevasses over the frontal region of the central flow unit (white dots in Fig. 5a). Crevasses also appeared at the margins of the sub-glacial valley.

By looking at the overall crevasse distributions in August 2012 and August 2013 (white dots in Fig. 5a and 5b) together with their corresponding *C* distributions (Fig. 4) we noticed that the outline of the densely crevassed region more or less follows the outline of the low friction region, indicating the governing role of basal friction on crevasse formation. This was also shown by the fact that there were more crevasses formed in the southern and middle frontal area in August 2013 than in August 2012 as the bed was more 'slippery' in August 2013 (Fig. 4b). The confining effects of the bed rock topography to the fast flow, basal friction and crevasse distribution also became more visible in the later stage of the surge: the modeled crevasses at the sub-glacial valley's sides indicated a sharper boundary in August 2013 than in August 2012.

4.3 Surface and basal water sources

We defined cut-through crevasses as crevasses that penetrate through 2/3 ice depth and assume that they could cut through the full depth of ice if filled with water and potentially route surface melt water into the basal hydrology system vertically.

We selected the cut-through crevasses in August 2012 and August 2013 (red dots in Fig. 5a and b) to identify possible routes of surface water to the bedrock. In August 2012 most of the crevasses in the frontal area cut through the ice deep enough and very likely represent future calving locations for the terminus during its advance. Most of the crevasses located between the northern and southern fast flowing regions were shallow, surface crevasses. Many crevasses above the margins of the sub-glacial valley could reach the bed and potentially route surface melt water from upstream to the bed. By August 2013 more cut-through crevasses had been developed in the lower southern and central basin compared with August 2012 as velocity gradients significantly increased after the basin-wide acceleration. There were more cut-through crevasses present above the shear margin but almost no cut-through crevasses above the over-deepening area.

Using the locations of cut-through crevasses above the margins of the sub-glacial valley that could potentially route surface melt water down to the bed, in August 2012 we calculated the sub-glacial water flow path according to the gradient of the hydraulic potential (Fig. 6a). The hydraulic potential (h) was calculated as below:

$$h = (z_s - z_b)\frac{\rho_i}{\rho_w} + z_b \quad (18)$$

in which z_s and z_b are surface and bedrock elevation; ρ_i = 910 kg m^{-3}and ρ_w = 1000 kg m^{-3} are the density of ice and water. The flow paths are generated by integrating through the vector field that follows the steepest descent in *h* using fourth-order Runge-Kutta method.

The surface melt water entering the bed at the north was predicted to either flow directly to the terminus, or stop at the sub-glacial over-deepening area (Sect. 2.1; Fig. 6a). Surface melt water entering the bed from the south was routed directly towards the terminus at the southern corner of the glacier, suggesting that surface melt contributed to the dramatic acceleration of the southern part of Basin 3 after the summer melt season in 2012.

In addition to the basal water supplied via the crevasse system, we also estimated the basal melt rate (Fig. 6b) for the temperate base area of the glacier. Within Elmer/Ice we computed the energy-balance at the bed from an estimated geothermal heat flux, strain heating and basal friction-heating (Gong et al., 2017). Relatively high basal melt rates (> 0.005 m a^{-1}) appeared at the side walls of the sub-glacial valley around the over-deepening area, mainly caused by frictional heating. The basal melt water followed similar patterns of flow as the surface melt water that reaches the bed.

5 Discussion

Previous studies of the surge in Basin 3 (Dunse et al., 2012, 2015; Gladstone et al., 2014) revealed an atypical surge activation phase with multi-decadal acceleration superimposed, for at least 6 years, by short-lived, abrupt seasonal speed-up events that were clearly related to summer melt., which could not be explained solely by the thermal switch mechanism (Murray et al., 2003) typical of polythermal surging glaciers in Svalbard.

We used the discrete element model – HiDEM (Åström et al., 2014) to locate the possible location of crevasses. In general the modeled crevasses distribution in August 2013 matches with the crevasses map derived from satellite observation. However there is a mismatch of the orientation in the middle upper area (Fig. 5c). It may be due to that HiDEM only simulates the ad-hoc formation but not the advection of crevasses, thus no crevasse formation history can be inferred from the model. The inclusion of crevasse advection could be implemented in a two-way coupling of HiDEM with a continuum model accounting for damage transport in future studies. The mismatch of the crevasse density (Fig. 5c) at the northern and southern frontal area could be caused by the mismatch of ice front position between reality and the model. Although in reality the ice front advanced for several kilometers after the full-surge, it was kept fixed in position in Elmer/Ice (Sect. 3.1). The shape and steepness of the ice front likely affects the behavior of the discrete element model. However, as they are concentrated at the terminus of the glacier, these crevasses are less likely to affect the basal hydrology system on a wider scale.

We then selected the modeled crevasses in August 2012 that may penetrate ice deep enough to act as routing-paths of surface melt water to the bed. In this study we focused on the cut-through crevasses formed above the margins of the sub-glacial valley because the basal flow pattern of the surface melt entering through those crevasses was indicative of potential subglacial water routing and hydrology.

We cannot directly simulate or quantify the effects of the surface melt water or basal melt water on the surge development due to the lack of a basal effective pressure dependent sliding relation. However, based on our results we can still present arguments to emphasize the role of crevasse, summer melt and basal hydrology system in the seasonal speed-up events.

Firstly, our calculation of the flow paths of both surface melt entering through the crevasses and basal melt water production suggest the potential of a direct lubricating effect acted beneath the northern and southern fast flow units. Figure 6 shows that

water entering through the crevasses downstream from the subglacial mountain (the flow paths in the northern half of Fig. 6a) will flow through the area where the northern fast ice flow unit has developed. The water accessing the bed at the southern part of the basin travels directly towards the terminus at the southern corner of the glaciated system, which has dramatically accelerated during the melt season in 2012.

Secondly, some of the basal water flow paths presented in Fig. 6a and 6b terminate under a plateau in the hydraulic potential which occurs in the over-deepened bedrock region (see also Fig. 1b). Given the very low gradients of our calculated hydraulic potential in this region and the presence of a local hydraulic potential minimum slightly downstream of the over-deepening, basal water would likely have low flow speeds, and possibly even accumulate in the over-deepened bedrock region, over time. This may have impacted on the surge development in Basin 3. Also given that the lowest basal resistance during most of 2012 (Fig. 4a) was immediately downstream of the over-deepening area in the northern flow unit, outflow of accumulated water likely enhanced the surge activation here. If seasonal surface melt water accumulates here and drains over a longer period, this may explain prolonged high ice velocities after the melt season has ended.

The temporary speed-up of the southern flow unit in 2008 (Gladstone et al., 2014) could plausibly have been triggered by an influx of basal water that was not repeated again until the basin wide surge was initiated. An outburst of basal water accumulated in the over-deepened bedrock region could provide one possible mechanism for this to occur. A ridge in hydraulic potential divides the northern and southern flow units in August 2012 (Fig. 6a). An anomalously high inflow of surface meltwater could have caused this ridge to be flooded if regular drainage channels were of insufficient capacity. We are unable to say how likely this is without a time series of surface melt data including the 2007 and 2008 seasons, but such an event could cause a temporary speed-up to the southern flow unit.

Englacial channels which may cause a redistribution of water within the hydrologic system (Fountain and Walder, 1998) are not directly considered in the current study. We assume that direct transfer of surface runoff via cut-through crevasses exceeds the englacial water transport at Basin 3.

Lastly, we look at the role of basal melt water in the activation of the southern flow unit. Basal meltwater from further upstream in the northern flow unit can drain toward the southern unit (Fig 6b; prior to the basin-wide surge, nearly all of the ice drained toward the northern flow unit). If this basal meltwater accumulated upstream due to the lower part of the glacier being below pressure melting point, such accumulated basal melt water could have caused the speed-up once basal temperatures reached melting point under the southern corner and the hydrologic system extended beneath the southern flow unit. Also basal melt water generated locally in the over-deepening area (Fig. 6b) may not have been able to drain completely in one season thus could be accumulated locally. However whether basal melt water can eventually burst out from the over-deepening area and contribute to the seasonal speed-up events or refreeze locally depends also on the development of the hydrology system and the thermal regime.

Although we lack either simulated or observed surface melt volumes for summer 2012 we would expect that the surface melt is much larger than basal melt. The runoff output from HIRHAM5 regional climate model in 1995 (personal information from R. Mottram of Danish Meteorological Institute; 1995 was not a year with high surface melt) at the location of the cut though crevasses was at least 10 time larger than the basal melt rate in either 1995 or 2012. The volume of surface melt observed at weather stations located in southwestern Basin 3 after summer in 2004 was also at least 10 times larger (Schuler et al., 2007). Considering the seasonal timings and magnitudes of speed-up events, and the feedback between surface melt water input and

hydraulic warming at the bed, it is clear that surface melt, when it can penetrate to the bed, causes a much higher impact on sliding and ice dynamics than basal melt water.

Then we also discuss the role of the crevasses formation in the long term acceleration. These are initiated as a consequence of extensional flow resulting from changes in the basal thermal structure in an early post-quiescent phase and act as the triggering and enhancing factor in the so-called 'annual hydro-thermodynamic feedback' proposed by Dunse et al. (2015). While Dunse et al. (2015) are unspecific as to the cause of "hydro-thermodynamic" initiation zone in the long term glacier acceleration, we propose that basal melt water resulting from the gradual thickening of ice (raising basal temperatures) during the quiescent phase, could sufficiently enhance flow speeds to initiate cut-through crevassing. The basal temperature distribution inversely calculated from the glacier geometry and velocity (Gong et al., 2016) showed a partially temperate bed in 1995 and expansion of the temperate region from 1995 to 2011, which is consistent with the presence of water at the bed. Given that basal meltwater fluxes are likely to be at least an order of magnitude lower than surface meltwater or runoff fluxes, basal melt probably has a relatively small influence on glacier sliding. We suggest that water at the bed, which is likely to be primarily routed toward the northern rather than southern flow unit due to topographic constraints (Fig. 6b), caused the speed up from the quiescent phase during the last part of the 20th century and early 21st century.

This would require two key developments from quiescent to surge phase. Firstly, the initiation of sliding after ice thickening provided sufficient insulation for the bed to reach pressure melting temperature and generate meltwater. This could have occurred during the early nineties. Then at some point before August 2012, extensional flow due to sliding became sufficient to cause cut-through crevasses leading to further acceleration and the surge onset due to the annual "hydro-thermodynamic" feedback. We have demonstrated that cut-through crevasses are likely to be present just prior to the surge in Basin 3, and that surface meltwater can flow along the paths corresponding to the regions of observed fast flow.

It is not clear at which point the "hydro-thermodynamic" feedback cut in, though it is likely to have first occurred in the northern flow unit, due to this unit's earlier acceleration. We suggest that the "hydro-thermodynamic" feedback cut in for the southern unit in 2011 or early 2012 due to crevasses penetrating near the southern margin (Fig. 5a), rapidly causing the basin wide surge.

Direct verification of the long term evolution of the surge active phase discussed above cannot be provided without quantification of the water reaching the bed and a basal sliding relation engaging the basal effective pressure. However our approach and results can throw some light on future studies of coupled ice dynamic/thermodynamic/hydrology simulations.

6 Conclusions

We have forced the discrete element model HiDEM with outputs from the continuum ice dynamic model Elmer/Ice to study the crevasse distribution during the surge in Basin 3, Austfonna ice-cap in 2012-2013. Our continuum to discrete multi-model approach provides simulated locations where cut-through crevasses allow surface melt water to be routed to the bed. We have demonstrated that automatic crevasse detection through Radon-transform may be used to validate simulated crevasse distribution from our continuum-discrete modelling approach. With the future addition of a basal hydrology model, the current study constitutes a step towards a fully coupled ice-dynamic englacial/basal hydrology modelling system in which both input locations of input surface water and basal meltwater generation are represented.

Our results support the "hydro-thermodynamic" feedback to summer melt proposed by Dunse et al (2015) to explain the seasonal speed-up in Basin-3 and the initiation of the acceleration of the southern flow unit in 2012. The calculated flow paths of the basal water according to hydraulic potential indicate either a direct enhancement to the ice flow through basal lubrication or a lagged-in-time mechanism through the outflow of accumulated water in the over-deepening area.

We propose that basal melt water production caused the speed up from the quiescent phase of Basin 3 during the last part of the 20th century and early 21st century. Then the "hydro-thermodynamic" feedback initiated during 2011 or early 2012 causing the activation of the southern flow unit and the expansion of the surge across the entire basin. The quantification of the roles and mechanisms involving basal melt water production, surface melt water and crevasse opening for the surge discussed in this study need to be further improved by coupling basal hydrology with the thermal regime evolution and surface mass and energy balance.

Author contribution. Y. Gong and T. Zwinger designed the numerical experiments and carried out the simulation in Elmer/Ice. J. Åström carried out the simulations in HiDEM. B. Altena produced the crevasse map with Radon-transform. T. Schellenberger processed and produced the TSX velocity time series. Y. Gong analyzed the model results and designed the figures. Y. Gong wrote the manuscript together with R. Gladstone, J. Moore and T. Zwinger. All the authors assisted in data interpretation and commented on/edited the paper.

Acknowledgements. We wish to thank all the partners for providing data and constructive discussion during the study, especially R. Mottram from Danish Meteorological Institute for the HIRHAM5 surface mass balance; T. Strozzi from GAMMA Remote Sensing and Consulting AG for the ERS-2 SAR surface velocity observation acquired in March to April 2011; M. McMillan from the University of Leeds for the surface elevation derived from Cryosat altimetry data acquired during July 2010 – December 2012; T. Dunse from the University of Oslo for the bedrock and ice thickness data and A. Kääb from the German Aerospace Center DLR (LAN_0211) for TSX data. We wish to thank F. Gillet-Chaulet from Laboratoire de Glaciologie et Géophysique de l'Environnement for making available his code for the inverse modelling. We also acknowledge CSC IT Center for Science Ltd. for the allocation of computational resources. The work was supported by Finnish Academy project 286587: Simulating Antarctic marine ice sheet stability and multi-century contributions to sea level rise. T. Zwinger is supported by the Nordic Center of Excellence eSTICC (eScience Tools for Investigating Climate Change in Northern High Latitudes) funded by Nordforsk (grant 57001). B. Altena is funded by the European Research Council under the European Union's Seventh Framework Programme grant agreement No. 320816. T. Schellenberger was funded by the Research Council of Norway (RASTAR, 208013), the Norwegian Space Centre as part of European Space Agency's PRODEX program (C4000106033), and the European Union FP7 ERC project ICEMASS (320816).

Reference

Åström, J., Timo, R., Tallinen, T., Zwinger, T., Benn, D., Moore, J. and Timonen, J.: A particle based simulation model for glacier dynamics, The Cryosphere, 7, 1591–1602, doi:10.5194/tc-7-1591-2013, 2013.

Åström, J., Vallot, D., Schäfer, M., Welty, E., O'Neel, S., Bartholomaus, T., Liu, Y., Riikilä, T., Zwinger, T., Timonen, J. and Moore, J.: Termini of calving glaciers as self-organized critical systems, Nat. Geosci., 7, 874–878, doi:10.1038/ngeo2290, 2014.

Benn, D., Gulley, J., Luckman, A., Adamek, A. and Glowacki, P.: Englacial drainage systems formed by hydrologically driven crevasse propagation, J. Glaciol., 55(191), 513–523, doi:10.3189/002214309788816669, 2009.

Bhardwaj, A., Sam, L., Singh, S. and Kumar, R.: Automated detection and temporal monitoring of crevasses using remote sensing and their implications for glacier dynamics, Ann. Glaciol., 57(71), doi:10.3189/2016AoG71A496, 2015.

Boon, S. and Sharp, M.: The role of hydrologically-driven ice fracture in drainage system evolution on an Arctic glacier, Geophys. Res. Lett., 30, doi:10.1029/2003GL018034, 2003.

Bougamont, M., Christoffersen, P., Hubbard, A., Fitzpatrick, A., Doyle, S. and Carter, S.: Sensitive response of the Greenland Ice Sheet to surface melt drainage over a soft bed, Nat. Commun., 5, doi:10.1038/ncomms6052, 2014.

Clark, G.: Thermal regulation of glacier surging, J. Glaciol., 16, 231–250, doi:10.1017/S0022143000031567, 1976.

Cook, S., Rutt, I., Murray, T., Luckman, A., Zwinger, T., Sel, N., Goldsack, A. and James, T.: Modelling environmental influences on calving at Helheim Glacier in eastern Greenland, The Cryosphere, 8, 827–841, doi:10.5194/tc-8-827-2014, 2014.

Copland, L., Sharp, M. and Nienow, P.: Links between short-term velocity variations and the subglacial hydrology of a predominantly cold polythermal glacier, J. Glaciol., 49, 337–348, doi:10.3189/172756503781830656, 2003.

Dowdeswell, J., Drewry, D. J., Cooper, A., Gorman, M., Liestol, O. and Orheim, O.: Digital mapping of the Nordaustlandet ice caps from airborne geophysical investigation, Ann. Glaciol., 8, 51–58, 1986.

Dunse, T., Greve, R., Schuler, T. V. and Hagen, J. O.: Permanent fast flow versus cyclic surge behaviour:numerical simulations of the Austfonna ice cap, Svalbard, J. Glaciol., 57, doi:10.3189/002214311796405979, 2011.

Dunse, T., Schuler, T. V., Hagen, J. O. and Reijmer, C.: Seasonal speed-up of two outlet glaciers of Austfonna, Svalbard,inferred from continuous GPS measurements, The Cryosphere, 6, 453–466, doi:10.5194/tc-6-453-2012, 2012.

Dunse, T., Schellenberger, T., Hagen, J. O., Kääb, A., Schuler, T. V. and Reijmer, C.: Glacier-surge mechanisms promoted by a hydro-thermodynamic feedback to summer melt, The Cryosphere, 9, 197–215, doi:10.5194/tc-9-197-2015, 2015.

Fountain, A. and Walder, J.: Water flow through temperate glaciers, Rev. Geophys., 36(3), 299–328, doi:8755-1209/98/97 RG-03579, 1998.

Gagliardini, O., Zwinger, T., Gillet-Chaulet, F., Durand, G., Favier, L., de Fleurian, B., Greve, R., Malinen, M., Martín, C., Råback, P., Ruokolainen, J., Sacchettini, M., Schäfer, M., Seddik, H. and Thies, J.: Capabilities and performance of Elmer/Ice, a new-generation ice sheet model, Geosci. Model Dev., 6, 1299–1318, doi:10.5194/gmd-6-1299-2013, 2013.

Gillet-Chaulet, F., Gagliardini, O., Seddik, H., Nodet, M., Durand, G., Ritz, C., Zwinger, T., Greve, R. and Vaughan, D.: Greenland ice sheet contribution to sea-level rise froma new-generation ice-sheet model, The Cryosphere, 6(6), 1561–1575, doi:10.5194/tc-6-1561-2012, 2012.

Gladstone, R., Schäfer, M., Zwinger, T., Gong, Y., Strozzi, T., Mottram, R., Boberg, F. and Moore, J.: Importance of basal processes in simulations of a surging Svalbard outlet glacier, The Cryosphere, 8, 1393–1405, doi:10.5194/tc-8-1393-2014, 2014.

Glen, J.: The Creep of Polycrystalline Ice, Proc. R. Soc., 228(1175), 519–538, doi:10.1098/rspa.1955.0066, 1955.

Gong, Y., Zwinger, T., Cornford, S., Gladstone, R., Schäfer, M. and Moore, J.: Importance of basal boundary conditions in transient simulations: case study of a surging marine-terminating glacier on Austfonna, Svalbard, J. Glaciol., 63(237), 106–117, doi:10.1017/jog.2016.121, 2016.

Lingle, C. and Fatland, D.: Does englacial water storage drive temperate glacier surges?, Ann. Glaciol., 36(7), 14–20, doi:10.3189/172756403781816464, 2003.

MacAyeal, D.: A tutorial on the use of control methods in ice sheet modeling, J. Glaciol., 39, 91–98, 1993.

McMillan, M., Shepherd, A., Gourmelen, N., Dehecq, A., Leeson, A., Ridout, A., Flament, T., Hogg, A., Gilbert, L., Benham, T., Michiel van den Broeke, Julian Dowdeswell, Xavier Fettweis, Brice Noël and Tazio Strozzi: Rapid dynamic activation of a marine-basedArctic ice cap, Geophys. Res. Lett., 41, 8902–8909, doi:10.1002/2014GL062255, 2014.

Moholdt, G. and Kääb, A.: A new DEM of the Austfonna ice capby combining differential SAR interferometry with ICESat laseraltimetry, Polar Res., 31, doi:10.3402/polar.v31i0.18460, 2012.

Möller, M., Finkelnhurg, R., Braun, M., Hock, R., Jonsell, U., Pohjola, V., Scherer, D. and Schneider, C.: Climatic mass balance of the ice cap Vestfonna, Svalbard: a spatially distributed assessment using ERA-Interim and MODIS data, J. Geophys. Res. Earth Surf., 116(F3), doi:10.1029/2010JF001905, 2011.

Morlighem, M., Rignot, E., Seroussi, H., Larour, E., Ben Dhia, H. and Aubry, D.: Spatial patterns of basal drag inferred using control methods from a full-Stokes and simpler models for Pine Island Glacier, West Antarctica, Geophys. Res. Lett., 37(14), doi:10.1029/2010GL043853, 2010.

Murray, T., Strozzi, T., Luckman, A., Jiskoot, H. and Christakos, P.: Is there a single surge mechanism? Contrasts in dynamics betweenglacier surges in Svalbard and other regions, J. Geophys. Res., 108(B5), 2237, doi:10.1029/2002JB001906, 2003.

Nick, F., van der Veen, C., Vieli, A. and Benn, D.: A physically based calving model applied to marine outlet glaciers and implications for the glacier dynamics, J. Glaciol., 56, 781–794, doi:10.3189/002214310794457344, 2010.

Nick, F., Vieli, A., Andersen, M., Joughin, I., Payne, A., Edwards, T., Pattyn, F. and van de Wal, R.: Future sea-level rise from Greenland's main outlet glaciers in a warming climate, Nature, 497, 235–238, doi:10.1038/nature12068, 2013.

Petrou, M. and Kadyrov, A.: Affine Invariant Features from the Trace Transform, IEEE Trans. Pattern Anal. Mach. Intell., 26, 30–44, doi:10.1109/TPAMI.2004.1261077, 2004.

Riikilä, T., Åström, J., Tallinen, T. and Timonen, J.: A discrete-element model for viscoelastic deformation and fracture of glacial ice, Comput. Phys. Commun., 195, 14–22, doi:10.1016/j.cpc.2015.04.009, 2015.

Roberts, J., Warner, R. and Treverrow, A.: Inferring ice-flow directions from single ice-sheet surface images using the Radon transform, J. Glaciol., 59, doi:10.3189/2013JoG12J042, 2013.

Robin, G.: Ice Movement and Temperature Distribution in Glaciers and Ice Sheets*, J. Glaciol., 2(10), 523–532, doi:10.3189/1955JoG2-18-523-532, 1955.

Sangwine, S. and Thornton, A.: Frequency domain methods. In: The colour image processing handbook, Springer US, Lond, UK and New York, USA., 1998.

Schäfer, M., Gillet-Chaulet, F., Gladstone, R., Pettersson, R., Pohjola, V., Strozzi, T. and Zwinger, T.: Assessment of heat sources on the control of fast flow of Vestfonna ice cap, Svalbard, The Cryosphere, 8, 1951–1973, doi:10.5194/tc-8-1951-2014, 2014.

Schellenberger, T., Dunse, T., Kääb, A., Schuler, T. V., Hagen, J. O. and Reijmer, C.: Multi-year surface velocities and sea-level rise contribution of the Basin-3 and Basin-2 surges, Austfonna, Svalbard, Cryosphere Discuss, doi:10.5194/tc-2017-5, 2017.

Schuler, T., Loe, E., Taurisano, A., Eiken, T., Hagen, J. O. and Kohler, J.: Calibrating a surface mass balance model for the Austfonna ice cap, Svalbard, Ann. Glaciol., 46, 241–248, doi:10.3189/172756407782871783, 2007.

Schuler, T., Dunse, T., Østby, T. and Hagen, J. O.: Meteorological conditions on an Arctic ice cap – 8 years of automatic weather station data from Austfonna, Svalbard, Int. J. Climatol., 34, 2047–2058, doi:10.1002/joc.3821, 2014.

Strozzi, T., Luckman, A., Murray, T., Wegmuller, U. and Werner, C.: Glacier motion estimation using SAR offset-tracking procedures, IEEE Trans. Geosci. Remote Sens., 40(11), doi:10.1109/TGRS.2002.805079, 2002.

Sundal, A. V., Shepherd, A., Nienow, P., Hanna, E., Palmer, S. and Huybrechts, P.: Melt-induced speed-up of Greenland ice sheet offset by efficient subglacial drainage, Nature, 469, 521–524, doi:10.1038/nature09740, 2011.

Toft, P. A. and Sørensen, J. A.: The Radon Transform-Theory and Implementation, Technical University of Denmark, Denmark. [online] Available from: https://www.dropbox.com/s/2ds08tgbjssw65q/1996_The%20Radon%20Transform-Theory%20and%20Implementation.pdf?dl=0, 1996.

van der Veen, C. J.: Fracture mechanics approach to penetration of surface crevasses on glaciers, Cold Reg. Sci. Technol., 27(1), 31–47, doi:10.1016/S0165-232X(97)00022-0, 1998.

van de Wal, R., Boot, W., van den Broeke, M., Smeets, P., Reijmer, C., Donker, J. and Oerlemans, J.: Large and Rapid Melt-InducedVelocity Changes in the AblationZone of the Greenland Ice Sheet, Science, 321(5885), 111–113, doi:10.1126/science.1158540, 2008.

Weertman, J.: Can a water-filled crevasse reach the bottom surface of a glacier?, IASH Publ., 95, 139–145, 1973.

Wesche, C., Jansen, D. and Dierking, W.: Calving Fronts of Antarctica: Mapping and Classification, Remote Sens., 5(12), 6305–6322, doi:10.3390/rs5126305, 2013.

Zwally, J., Abdalati, W., Herring, T., Larson, K., Saba, J. and Steffen, K.: Surface Melt-Induced Acceleration of Greenland Ice-Sheet Flow, Science, 297(5579), 218–222, doi:10.1126/science.1072708, 2002.

Table 1 TerraSAR-X acquisitions of Basin 3 and repeat-pass period

Repeat-pass period (days)	Start and end-date
11	19 Apr 2012–30 Apr 2012
11	30 Apr 2012–11 May 2012
88	11 May 2012–7 Aug 2012
11	7 Aug 2012–18 Aug 2012
11	18 Aug 2012–29 Aug 2012
44	29 Aug 2012–12 Oct 2012
11	12 Oct 2012–23 Oct 2012
11	23 Oct 2012-3 Nov 2012
22	3 Nov 2012–25 Nov 2012
11	25 Nov 2012–6 Dec 2012
22	6 Dec 2012–28 Dec 2012
11	28 Dec 2012–8 Jan 2012
22	8 Jan 2013–30 Jan 2013
11	30 Jan 2013–10 Feb 2013
22	10 Feb 2013–4 Mar 2013
11	4 Mar 2013–15 Mar 2013
22	15 Mar 2013–6 Apr 2013
11	6 Apr 2013–17 Apr 2013
22	17 Apr 2013–9 May 2013
11	16 Aug 2013–27 Aug 2013
11	12 Nov 2013–23 Nov 2013
15	23 Nov 2013-8 Feb 2014
11	8 Feb 2014-19 Feb 2014
77	19 Feb 2014-7 May 2014
11	7 May 2014-18 May 2014
55	18 May 2014-12 July 2014
11	12 July 2014-23 July 2014

610

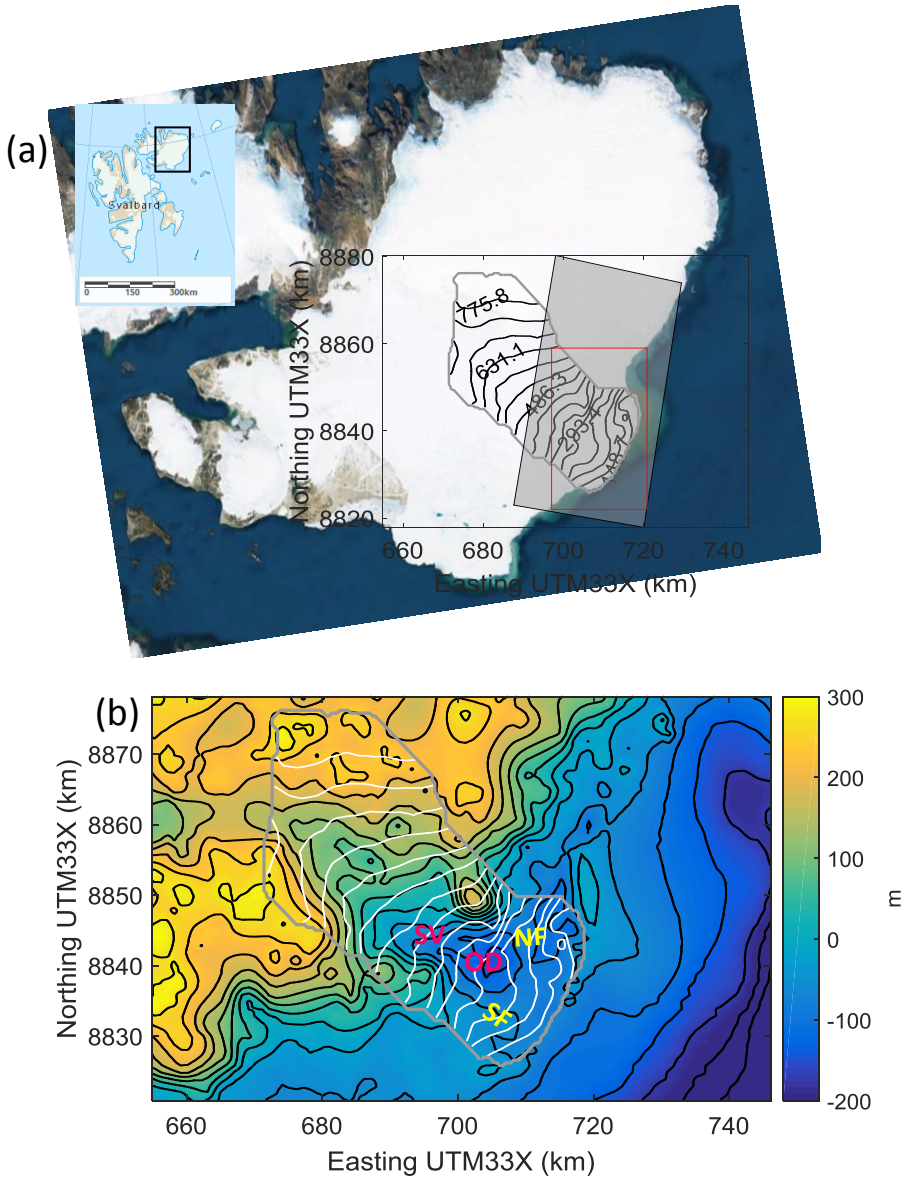

Figure 1. Surface and bedrock topography of Basin 3, Austfonna. (a) Surface elevation of Basin 3 contours with solid black lines (with ~48.2 m interval), on top of a satellite image of Nordaustlandet from TerraColor® Global Satellite Imagery (http://www.terracolor.net/). The gray transparent box shows the coverage of the TerraSAR-X scene (30 April 2012). The model domain of HiDEM is outlined with red box. The insert at the upper left corner shows the ice cap's location within the Svalbard archipelago; (b) Bedrock topography is color-coded, contoured with black solid line with a ~37.1 m interval and superimposed by surface elevation contours (white solid line with ~ 48.2 m interval). The gray solid line outlines Basin 3 and the model domain of Elmer/Ice in both panels.
'SV' marks the subglacial valley that runs between two bedrock maxima in the northeast and southwest and extends several tens of kilometers upstream and downstream. 'OD' marks the minimum bedrock height for Basin 3 and is within an over-deepening in the lower part of the valley. 'NF' marks the downstream area of the northern flow unit of the glacier, which runs from the upstream of the valley and exits from the northern terminus. The alignment of these labels roughly indicates the flow direction. Similarly, 'SF' marks the downstream area of the southern flow unit.

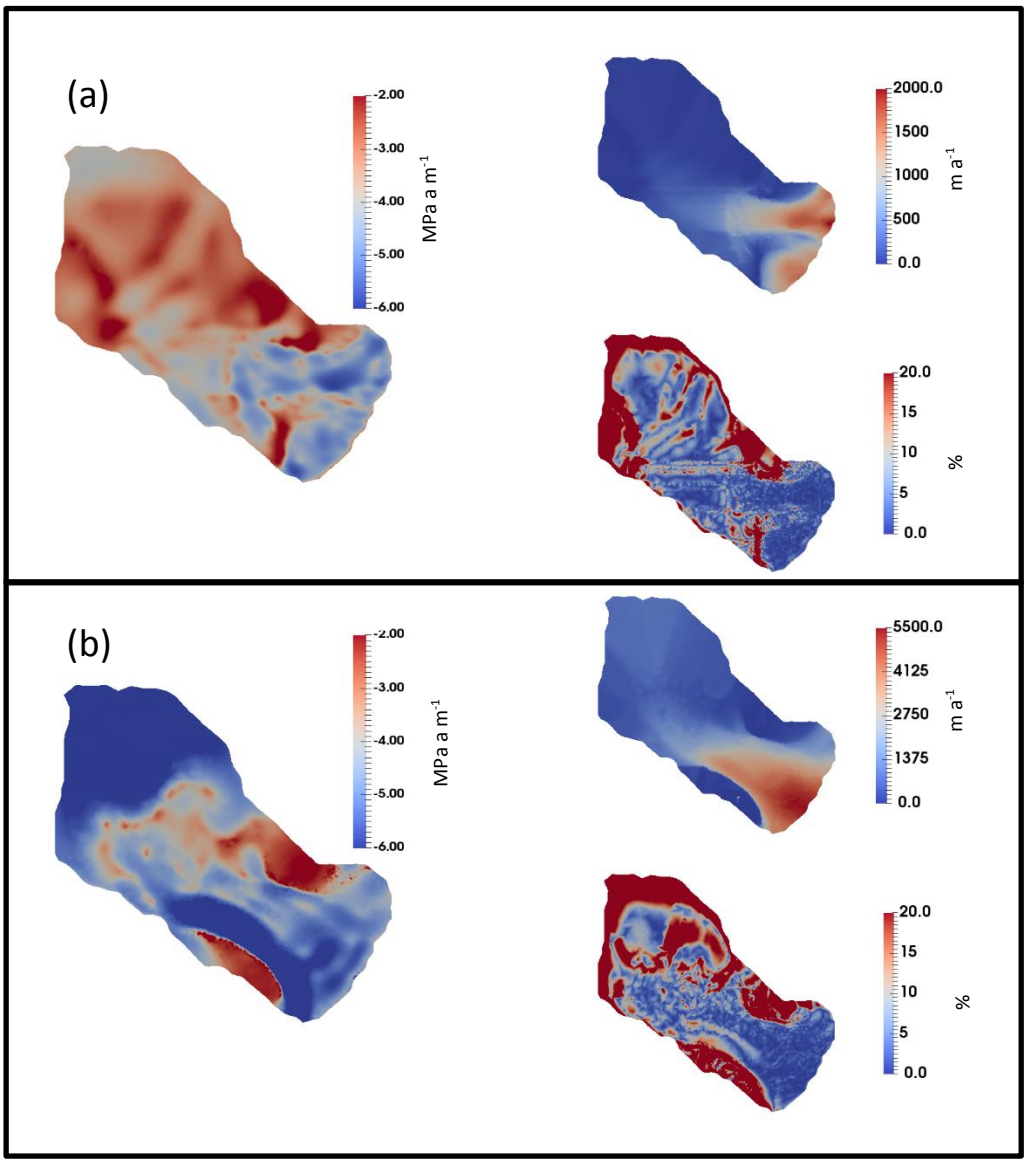

Figure 2. Basal friction coefficient inverted from surface velocity data in (a) 18-29 August 2012 (C_{pre}) and (b) 16-27 August 2013 (C_{post}). Both panels display basal friction coefficient shown onto the left, surface velocity data after post-processing (Sect. 2.2) shown on the upper right and the relative difference between observed and modeled surface velocity magnitude shown on the lower right.

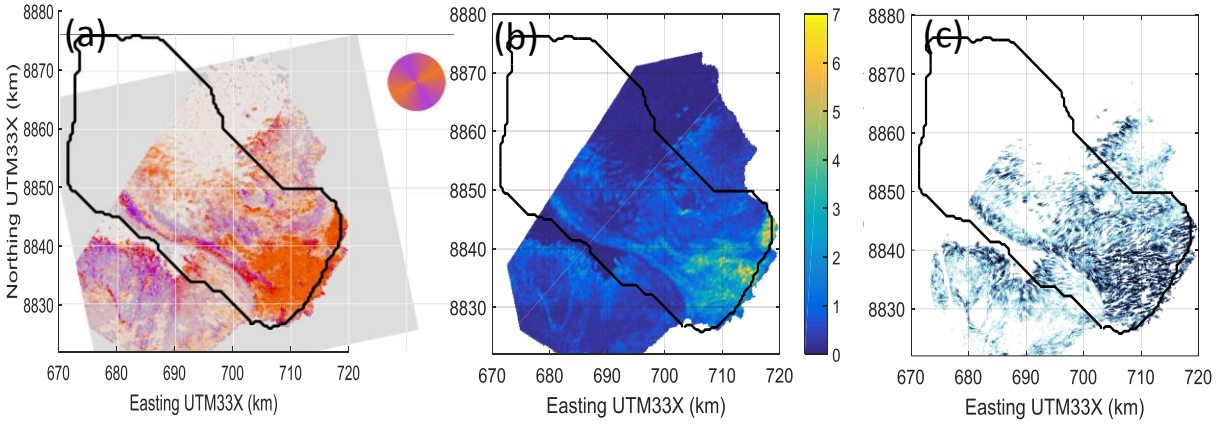

Figure 3. The crevasse maps created from Radon-transform. (a) The orientation of crevasses indicated by a color wheel, in which the strength of the signal controls the saturation; (b) The highest responding orientation from the Radon-transform ($\tilde{s}(\theta)$) with the color bar indicating the intensity; (c) The cartographic map indicating both the orientation and intensity of the two strongest responding orientations. Basin 3 is outlined by black solid line.

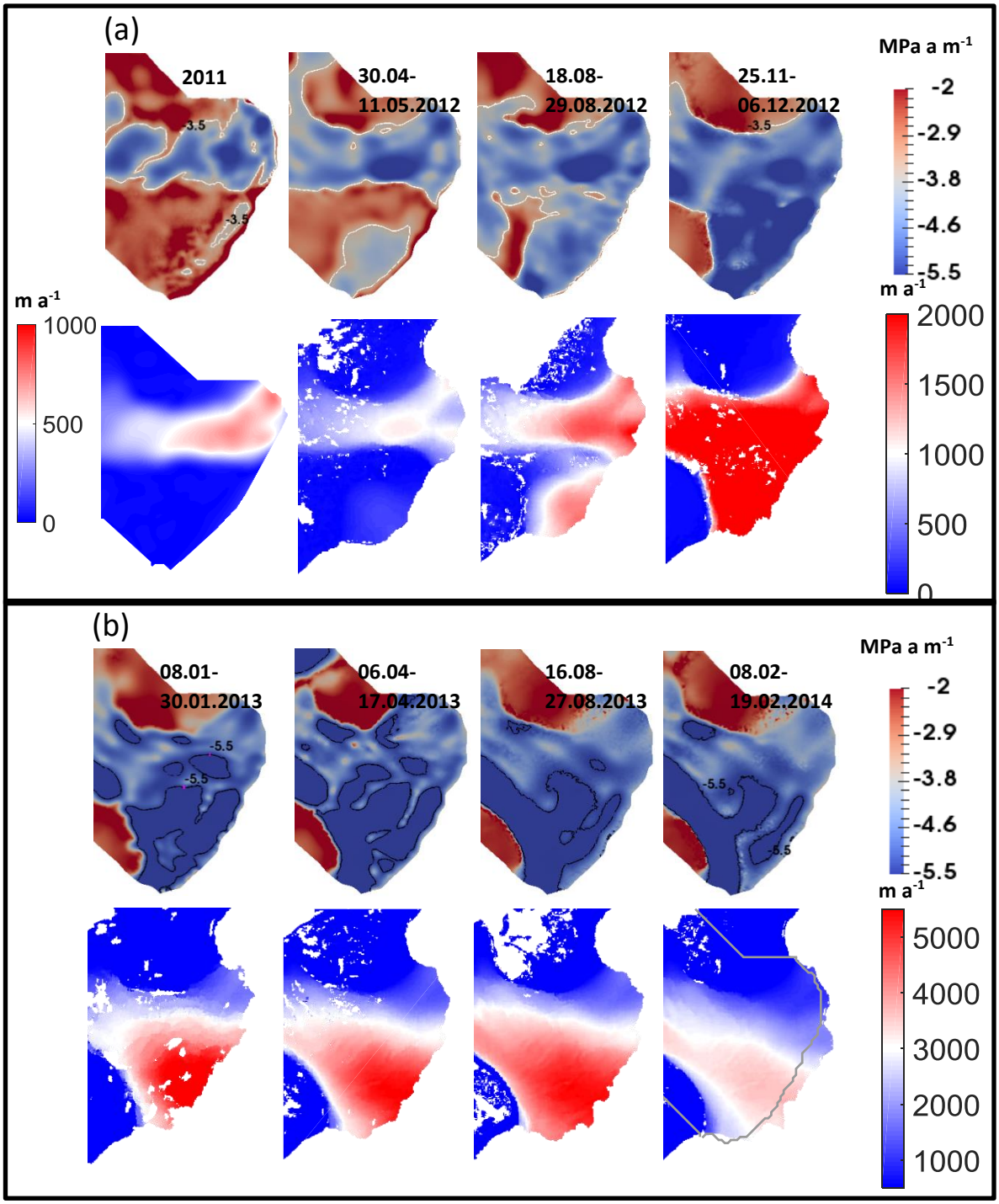

Figure 4. The evolution of basal friction coefficient (C), with the corresponding observed speeds plotted below, shown for the model domain of HiDEM. (a) $\log_{10}(C)$, overlain with white contour lines showing $\log_{10}(C)$ = -3.5 (low friction), from the time before the peak of the surge. (b) $\log_{10}(C)$, overlain with black contour lines showing $\log_{10}(C)$= -5.5 (almost vanishing friction), from the time period at and after the peak of the surge. The speed in 2011 was acquired from ERS-2 SAR imagery (color bar on the left). The rest of the speeds snapshot were from TSX SAR (color bar on the right). The grey solid line outlines the Basin 3 boundary.

615

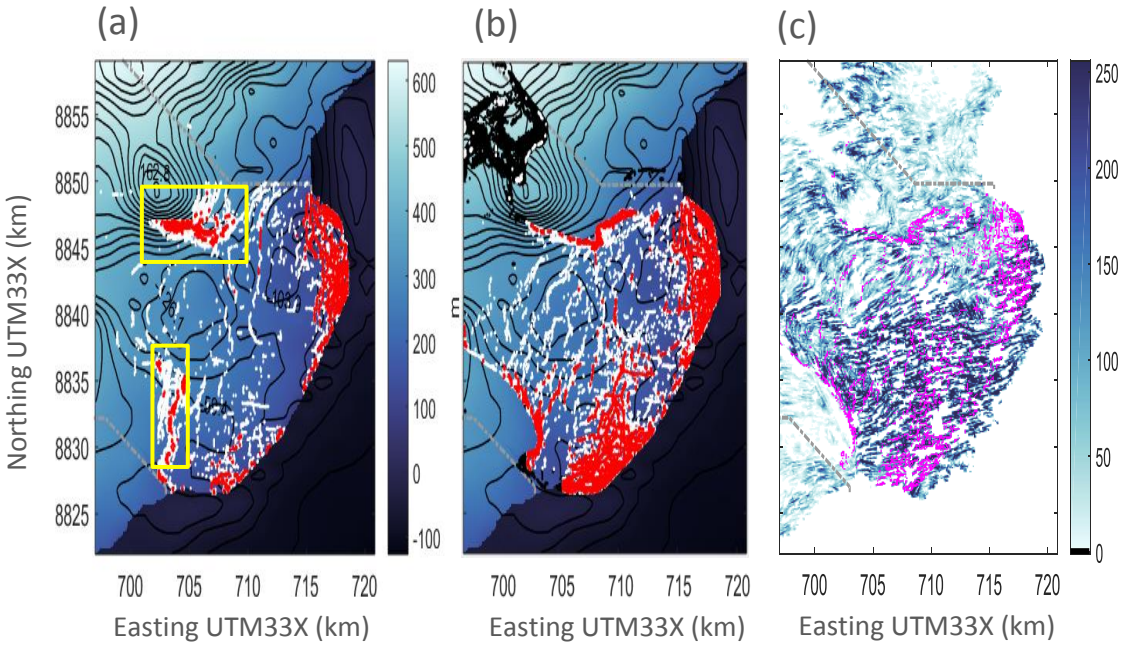

Figure 5. Crevasse distribution from HiDEM on (a) August 2012 and (b) August 2013 and (c) satellite observation. The color of the underlying image in (a) and (b) shows the surface elevation of the glacier. Bedrock topography contours are shown in black with a ~23.7 m interval. All the dots in both (a) and (b), regardless of the color, indicate the modeled crevasse distribution from HiDEM. The red dots are the cut-through crevasses. The red dots in the yellow boxes in (a) are the ones referred as cut-through crevasses above the sub-glacial valley margins and are used for calculating the flow paths of the surface melt reached the bed. The black dots in (b) (upper left and lower left corner) mark crevasses produced due to boundary effects in the model (Sect. 4.2). They are eliminated from the crevasse map. The rest of the crevasses are marked with white dots, and are mostly shallow crevasses, hence irrelevant to water routing. The cartographic representation of the observed crevasse orientation on 8 August 2013 is shown in (c) (color-coded with detecting intensity in the background). The magenta color shows the area where modeled and observed crevasse match. The basin side boundary is outlined with gray dashed line in all the sub-plots.

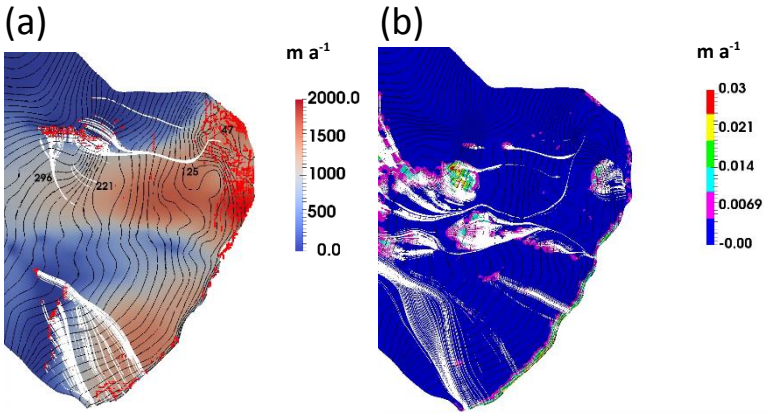

Figure 6. The flow paths of different water sources derived from the results in August 2012. (a) The white lines indicate the path of surface melt water after entering the basal hydrology system via cut-through crevasses (red dots) according to hydraulic potential. The modeled basal velocity magnitude is color-coded in the background. (b) The white lines indicate the water path of basal melt water from locations with in-situ melt rates above 0.005 m a^{-1}. The colored contour lines indicate the value of the basal melt rate. The black contour lines in both (a) and (b) indicate the hydraulic potential.